ADVANCED QUANTUM TECHNOLOGIES
www.advquantumtech.com

A 3D Polymeric Platform for Photonic Quantum Technologies

*Maja Colautti, Pietro Lombardi, Marco Trapuzzano, Francesco S. Piccioli, Sofia Pazzagli, Bruno Tiribilli, Sara Nocentini, Francesco S. Cataliotti, Diederik S. Wiersma, and Costanza Toninelli**

The successful development of future photonic quantum technologies will much depend on the possibility of realizing robust and scalable nanophotonic devices. These should include quantum emitters like on-demand single-photon sources and non-linear elements, provided their transition linewidth is broadened only by spontaneous emission. However, conventional strategies to on-chip integration, based on lithographic processes in semiconductors, are typically detrimental to the coherence properties of the emitter. Moreover, such approaches are difficult to scale and bear limitations in terms of geometries. Here an alternative platform is discussed, based on molecules that preserve near-Fourier-limited fluorescence even when embedded in polymeric photonic structures. 3D patterns are achieved via direct laser writing around selected molecular emitters, with a fast, inexpensive, and scalable fabrication process. By using an integrated polymeric design, detected photon counts of about 2.4 Mcps from a single cold molecule are reported. The proposed technology will allow for competitive organic quantum devices, including integrated multi-photon interferometers, arrays of indistinguishable single-photon sources, and hybrid electro-optical nanophotonic chips.

1. Introduction

Future quantum technologies rely on light manipulation at the single photon level, targeting unmatched functionalities based on quantum effects.[1] In this context, quantum emitters hold promise for the realization of on-demand sources of non-classical light[2] and for measurements beyond the classical limit.[3] To this end, the required efficiency in processing and detecting quantum states can be promoted by an effective coupling of quantum emitters to photonic structures.[4] The nanofabrication of semiconductor hybrid devices, for instance, has shown compelling results, while proving the integration to be demanding and hardly scalable.[5,6] Moreover, structuring the environment around quantum emitters at the wavelength scale also affects the emission properties of the emitter, typically degrading its quantum coherence and photostability.[7,8]

Polymers, being low-cost mass-produced materials with tailored physical, electronic, and optical properties, are widely used in nanotechnology and biomedicine.[9] They provide new interesting functionalities for optoelectronic and photonic devices,[10] allowing for fully 3D circuit design and free-standing structures, while at the same time supporting hybrid integration[11] and inter-chip connections.[12] Seminal results reported in refs. [13–18] point at the key advantages of single-emitter integration in polymeric microstructures: one-step 3D patterning and a-priori positioning of the emitter in high-intensity regions of the electro-magnetic field. Nevertheless, the colloidal systems employed in refs. [13–15,17,18] are typically subject to decoherence and spectral diffusion,[7,19] whereas the epitaxially grown quantum dots in ref. [16] are not favorable to a 3D integration.

Dr. M. Colautti, Dr. S. Nocentini, Prof. F. S. Cataliotti, Prof. D. S. Wiersma, Dr. C. Toninelli
European Laboratory for Non-Linear Spectroscopy (LENS)
Via Nello Carrara 1, Sesto Fiorentino 50019, Italy
E-mail: toninelli@lens.unifi.it

The ORCID identification number(s) for the author(s) of this article can be found under https://doi.org/10.1002/qute.202000004

DOI: 10.1002/qute.202000004

Dr. M. Colautti, Dr. M. Trapuzzano, Dr. S. Pazzagli, Prof. F. S. Cataliotti, Prof. D. S. Wiersma
Dipartimento di Fisica e Astronomia
Università degli Studi di Firenze
Via G. Sansone 1, Sesto Fiorentino 50019, Italy

Dr. P. Lombardi, Dr. F. S. Piccioli, Dr. S. Pazzagli, Dr. S. Nocentini, Prof. F. S. Cataliotti, Dr. C. Toninelli
National Institute of Optics (CNR-INO)
Largo Enrico Fermi 6, Firenze 50125, Italy

Dr. B. Tiribilli
Institute for Complex Systems (CNR-ISC)
Via Madonna del Piano 10, Sesto Fiorentino 50019, Firenze, Italy

Prof. D. S. Wiersma
Istituto Nazionale di Ricerca Metrologica (INRiM)
Torino IT-10135, Italy

Single organic molecules of polyaromatic hydrocarbons (PAHs) have shown remarkable quantum optical properties within numerous combinations of guest chromophores and host matrices, and are potentially compatible with polymer chemistry. In particular, anthracene nanocrystals doped with dibenzoterrylene molecules (DBT:Ac NCs), exhibiting photostable single-photon emission and near to lifetime-limited linewidths at 3 K,[20] are suitable for the integration in polymeric devices.[21,22] As co-authors in ref. [22], some of us have shown, for instance, that electron-beam lithography on NCs-doped polymers is a convenient way to fix their position on previously patterned semiconductor chips. However, the fabrication of all-organic quantum photonic devices call for high-resolution, single-step, full-3D patterning and selective integration of molecular quantum emitters.

In this work we demonstrate such a self-contained and versatile quantum photonic platform, based on the integration of single molecules in 3D polymeric optical elements, supporting efficient and near to lifetime-limited emission. The nanophotonic chips are obtained by direct laser writing (DLW) of polymers,[23] with unique advantages in terms of versatility, availability of a broad range of multi-purpose photoresists, sub-micron resolution,[24] and computer-aided manufacturing. The compatibility with molecules and broad flexibility in the design is demonstrated here by embedding anthracene nanocrystals doped with dibenzoterrylene molecules at variable heights and well-defined locations in different polymer architectures, fabricated either on silica or gold substrates. Critical aspects, like the performance of the device under cryogenic cooling and the influence of the fabrication process on the quantum coherence of the emitter, are investigated. In particular, close-to Fourier limited emission is observed from on-chip molecules at cryogenic temperatures and enhanced light extraction is achieved, using a micro-dome solid immersion lens design. The concept introduced in this paper can offer unique solutions for future photonic quantum devices, combining on a single chip a 3D polymeric architecture with the optimal properties of single-photon emission from fluorescent molecules.

2. Organic Quantum Emitters in 3D Polymeric Structures

Single PAHs are excellent candidates as non-classical light sources,[25–29] non-linear elements at the few photon level,[30–32] and nano-scale sensors for electric fields, pressure, and strain.[33–38] Recently they have been successfully integrated in open optical cavities[32,39] and antennas,[40] and evanescently coupled to nanoguides[36,41] and waveguides.[42–44] Here, in **Figure 1**, we present three different light collecting devices, 3D-carved in polymers, and each fully embedding a nanocrystal with fluorescent molecules. In the respective artistic views (top panels 1a,b,c), the integrated emitter is represented by a dipole (black arrow) and red arrows highlight the promoted direction for the emitted fluorescence. Figure 1a shows a micro-dome on a transparent dielectric substrate (silica, refractive index $n = 1.45$). This is a modified Weierstrass solid immersion lens (SIL),[45,46] consisting of a hemisphere and a cylindrical base built on top of one DBT:Ac NC. NCs doped with multiple DBT molecules are previously deposited on the substrate (grey in the figure) and selectively addressed, based on a preliminary characterization of the fluorescence at room temperature. The structure is therefore centered on the emitter, so as to maximize upwards redirection and collection efficiency at narrow angles. Figure 1b shows a similar design, this time realized on a gold-coated layer (~200 nm thick), to avoid radiation in the lower hemisphere. Thanks to the non-linear polymerization enabled via DWL, suspended architectures can also be fabricated, such as the arch waveguide drawn in Figure 1c. In this case the nanocrystal is completely enveloped at the middle-point of the structure, to efficiently route fluorescence throughout the silica substrate. The suspended architecture helps improving the coupling efficiency[15] and avoids losses through the substrate, determined by the low refractive index of the polymer material. A correct emitter position in the vertical dimension is ensured by the use of two photoresist layers with different viscosity but equal refractive indices. The accurate reproduction of the three designs can be appreciated in the scanning electron microscope images reported in Figures 1d–f. In Figure 1e, the standing wave pattern at the surface of the micro-dome, especially visible nearby the substrate and not present in Figure 1d, is a result of the writing-laser back reflection from the gold substrate.[47] This forms with the incoming beam an interference pattern, which is impressed in the polymerized volume, with a pitch $\lambda/2n \approx 256$ nm, where $\lambda = 780$ nm is the writing-laser wavelength and $n = 1.52$ the refractive index of the photoresist. In particular, the undercut below the structure arises in correspondence to the first node of the interference pattern, at the substrate interface.

For each structure, fluorescence imaging has been used to evaluate the persistence of molecular emission. Figure 1g–i represents the fluorescence maps in real space at room temperature. They have been collected from the top and through the substrate in the first two cases and in the waveguide geometry, respectively (see Experimental Section). The dashed line in the figures outlines the physical contour of the respective structure. The presence of fluorescence in all the devices of Figure 1 is the first fundamental evidence for the compatibility of the organic molecular emitters with the whole fabrication process, both on dielectric and metallic surfaces and even in the suspended architecture. Notably, after an optimization of the writing parameters, all the fabricated micro-dome devices showed emission from the embedded molecules. The integration success rate is also enhanced by defining and anchoring the coordinate system of the writing-laser beam to the location of selected nanocrystals within the optical microscope image. Deterministic positioning with such a simple and cost-effective fabrication method is key for scaling up the process to more complex chips, for example, with multiple emitters.

We would like to note that the overall process of the nanocrystals' growth, deposition, and selection of single photon sources requires less than one hour and can be readily automated. In particular, NCs are held in an aqueous suspension that results from reprecipitation, following the injection of a mixed Ac and DBT solution into sonicating water (see Experimental Section and ref. [20,48] for further details). The NCs are hence deposited on the sample via dessication after drop-casting the suspension. Finally, the overall fabrication of the polymeric photonic structure, including sample preparation, writing of the dome/waveguide

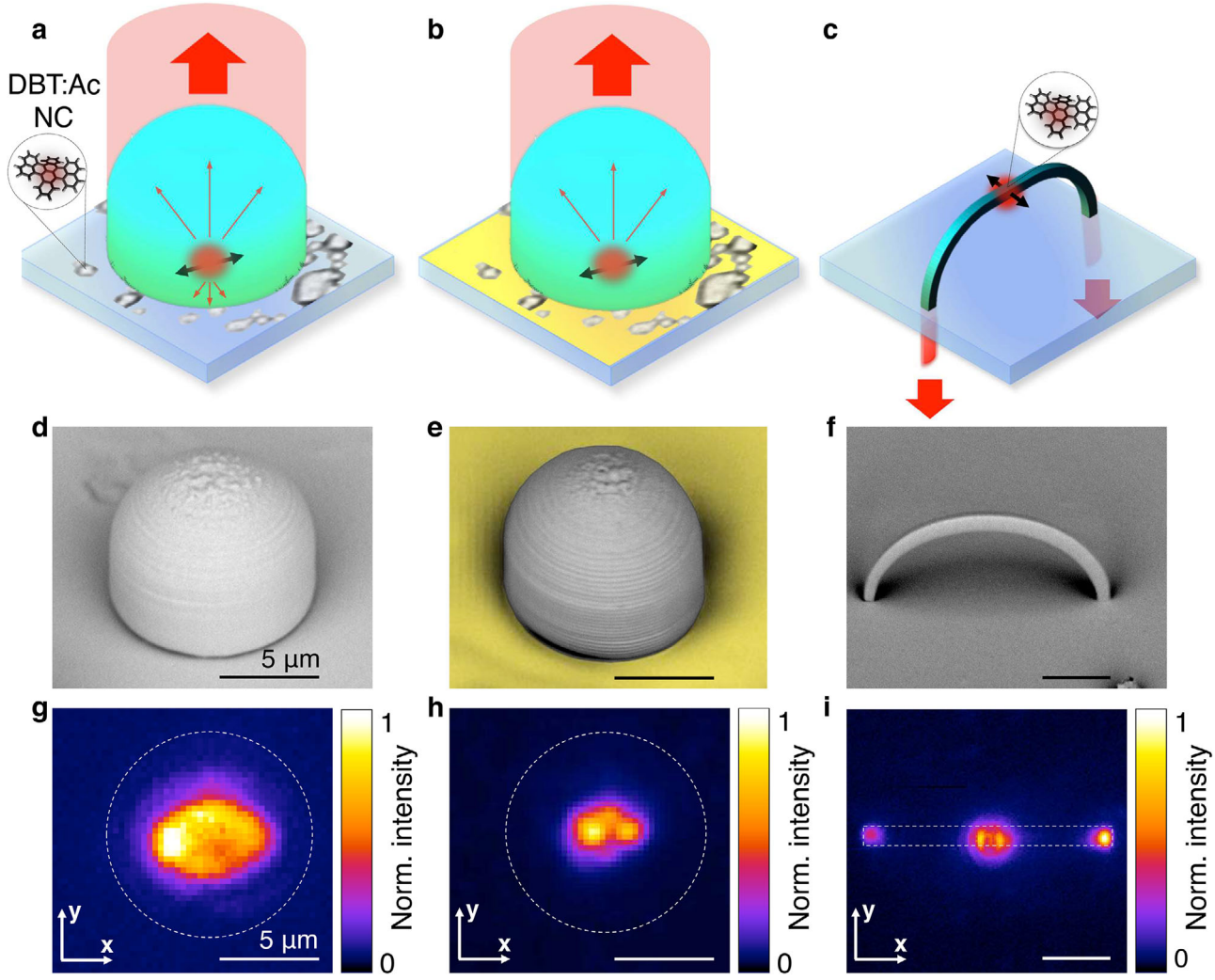

Figure 1. 3D integration of organic quantum emitters in a polymeric platform. Top panel: Artistic views of three light collecting devices realized with Direct Laser Writing and fully embedding an anthracene nanocrystal with fluorescent molecules of dibenzoterrylene (DBT:Ac NC). The black double arrow represents the dipolar emitter and red arrows highlight the promoted direction for the emitted fluorescence. a,b) Micro-dome lens design for upwards redirection, respectively realized on a silica substrate, and on a gold-coated layer to avoid bottom radiation and maximize collection efficiency. c) Suspended arch waveguide, fully enveloping the nanocrystal at its middlepoint, for efficient routing of fluorescence throughout the silica substrate. d–f) Scanning Electron Microscope images of the respective structures. g–i) Fluorescence maps attesting the persistence of molecular emission after fabrication, acquired at room temperature and collected from the top in the micro-dome designs (d,e) and through the substrate in the waveguide geometry (f). The dashed line in the maps denotes the contour of the respective structure.

device and development, is completed within less than one hour time (see Experimental Section).

The bright spots in Figure 1g,h correspond to emission from the nanocrystals at the bases of the micro-domes. In Figure 1i instead, fluorescence is observed both in correspondence with the nanocrystal position at the center of the waveguide, and at the lateral output ports, where the guided emission is out-coupled. From the relative intensities, a lower bound for the molecule-to-waveguide coupling efficiency can be hence estimated, yielding a value of about 10%, considering both directions in the waveguide. We remark that this measurement at room temperature is the result of the integrated signal from all the emitters in the NC, each with different orientation and position with respect to the guided mode, hence with varying coupling efficiency. Furthermore, the additional propagation losses due to the emitter inclusion can be evaluated by comparing the normalized laser throughput ($\eta_{WG+NC} = 36 \pm 1\,\%$) with the case of undoped waveguides ($\eta_{WG} = 40 \pm 2\%$). A 10%-measured value for the additional scattering losses is encouraging and can be further minimized upon selection of smaller nanocrystals, for example, by integrating fluorescence imaging capability in the DLW workstation, as done in ref. [15].

In the following, more accurate experiments on the geometry depicted in Figure 1b are discussed, characterizing the emission at the single molecule level and in a cryogenic environment. Indeed, in the context of quantum technologies, coherence in the emission of single photons is required for basic quantum optics operations, whereas narrow lines enable sensing

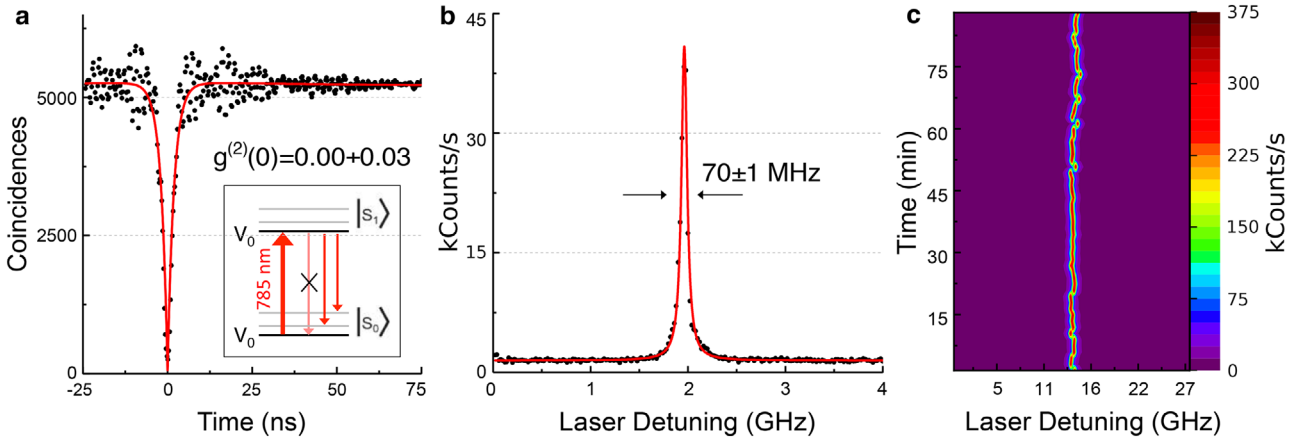

Figure 2. Optical characterization of the integrated emitters at cryogenic temperature. Measurements are performed on the micro-dome on gold structure. Inset: Simplified Jablonski diagram of the pumping scheme. The zero-phonon line of a single DBT molecule is selected in frequency with a tunable continuous-wave laser (≈ 785 nm) and the Stokes-shifted fluorescence is collected through a longpass filter. a) Histogram of photon coincidences on two avalanche photodiodes in a Hanbury Brown and Twiss configuration. The second order autocorrelation function at zero delay is inferred by the best fit (red line) to the experimental data (black dots), yielding $g^{(2)}(0) = 0.00 + 0.03$. b) In the excitation spectrum the Stokes-shifted fluorescence is recorded as a function of the laser frequency. The Lorentzian fit (red line) to the experimental data (black dots) yields a FWHM $\gamma_{exp} = 70 \pm 1$ MHz. c) Photostability of the integrated molecule emission shown by repeated linewidth measurements. No background subtraction has been applied to the reported measurements.

applications and efficient interfacing with atomic or ion-based memories.[49] Such properties can be observed with a standard epifluorescence microscope, cooling the sample down to 3 K (see Experimental Section). The employed pumping scheme is shown in the simplified Jablonski diagram in the inset of **Figure 2**a. By scanning the frequency of a tunable continuous-wave diode laser around a wavelength of ≈785 nm, the zero-phonon line of a single DBT molecule within a highly doped nanocrystal can be selected. The Stokes-shifted fluorescence is collected through a longpass filter and analyzed in different aspects. No background subtraction has been applied to the reported measurements.

The emitted photon statistics is measured with two fiber-coupled avalanche photodiodes (SPADs) arranged in a Hanbury Brown and Twiss (HBT) configuration. The second order autocorrelation function $g^{(2)}(\tau)$ is inferred from the histogram for short delay times of the photon coincidences on the two SPADs. A typical result from the micro-dome on gold structure is displayed in Figure 2a, obtained pumping with a saturation parameter equal to 1. The best fit to the experimental data with the function $g^{(2)}(\tau) = 1 - be^{-|\tau|\Gamma}$, where τ is the time delay and Γ accounts for the excitation and spontaneous emission rates, yields $g^{(2)}(0) = 0.00 + 0.03$. Such value clearly verifies single molecule emission and proves the high purity of the single photon stream emitted in the integrated-molecule geometry.

By recording the Stokes-shifted fluorescence as a function of the laser frequency, operating well below saturation, the excited state population is probed and the zero-phonon linewidth can be directly retrieved. A characteristic excitation spectrum is shown in Figure 2b, with linewidth $\gamma_{exp} = 70 \pm 1$ MHz, close to the lifetime limit. Such value for γ_{exp} is equal to the result for non-integrated DBT:Ac NCs at 3 K, given its statistical distribution,[20] and corresponds to approximately 1.9 times the theoretical Fourier-limit (38 MHz). We can hence deduce that this fabrication process does not alter significantly the NC properties and that quantum coherence is not compromised.

Finally, spectral diffusion is investigated by repeating the linewidth measurement previously described over time, for 1.5 h. Figure 2c shows a good photostability of the integrated molecule emission, whose excitation central frequency fluctuates within the range of few linewidths. These results are a relevant indication that the proposed polymeric platform is a reliable technique to embed single molecules in a photonic circuit.

3. Enhanced Collection at Low Temperature from a Single Molecule

We choose the micro-dome design as a case study to investigate its performances in terms of light extraction from single molecules. The total height of the structure is given by $h = (1 + 1/n)r$, where n is the polymer refractive index and r the radius of curvature. This design provides redirection via refraction at all upwards angles and efficiently compresses emission into a small numerical aperture. It also offers advantages in terms of simplicity of fabrication and robustness against imperfections. The structure dimensions are optimized assuming a dipole-to-gold distance $\text{dipole}_h = 100$ nm (which promotes emission in the upper hemisphere following ref. [40]), yielding $h_{th} = 8.7$ µm and $r_{th} = 5.3$ µm. The DBT alignment within the Ac crystal is well known and lies horizontally on the plane of the substrate.[27] However, since there is no experimental control over the fluorophore position within the NC volume, calculations are performed varying its value within the largest possible NC thickness of 400 nm.

In **Figure 3**, the results of 2D numerical simulations for the collection efficiency and the collected photon flux (for the experimental numerical aperture $NA \sim 0.62$) for the micro-dome

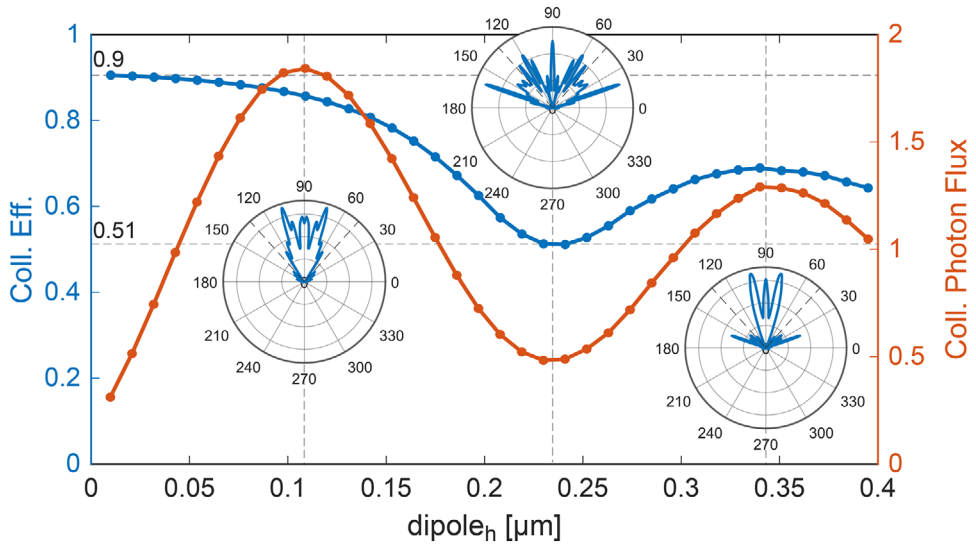

Figure 3. 2D numerical simulation of the micro-dome geometry. Collection efficiency and collected photon flux calculated as a function of the fluorophore vertical position within the nanocrystal volume (dipole$_h$), for the the micro-dome on gold. The collected photon flux is calculated as the the ratio between the radiated power within the numerical aperture acceptance $NA \sim 0.62$ and the total power emitted in a homogeneous medium. Polar plots corresponding to three dipole positions are added as insets to the figure, with grey dashed lines indicating the nominal maximum collection angle.

geometry on gold are summarized (see Experimental Section). Although related to the emission in the orthogonal plane to the dipole orientation, our results are qualitatively comparable with earlier 3D simulations.[46] For dipole$_h \approx 100$ nm, our numerical results predict a collection efficiency of more than 85%, together with a small enhancement of the total emission rate. In the corresponding polar plot, the emission pattern appears highly directional, resulting in $\sim 80\%$ of the total emission funneled within a polar angle of about 30°. The oscillatory behavior in the detected photon flux is due to the interference nature of the photonic redirection effect, as already discussed for a similar case, for example, in ref. [40]. Close to the metal layer, the dipolar emission is obviously quenched. As the dipole position is further displaced away from the gold surface, the onset of emission lobes beyond the critical angles is clearly visible in the second polar plot, reducing the overall collection efficiency, even when constructive interference in the forward direction is recovered for dipole$_h \simeq 350$ nm.

Based on such calculated results, the fabrication of the micro-dome on gold embedding a single DBT:Ac NC was optimized and characterized by means of atomic force microscopy (AFM). A typical AFM image is displayed in **Figure 4**a. In particular, a strip-scan of the structure passing through the dome pole is shown together with a high resolved AFM map of the top 4×4 μm^2 surface area. From the dome profile, we estimate the experimental dimensions of the structure, with a total height $h = 9.1 \pm 0.1$ μm and a radius $r = 5.0 \pm 0.1$ μm, in good agreement with the nominal values set by the numerical optimization. From the AFM map, the average surface roughness is estimated to be $\Delta r = 41 \pm 4$ nm.

Figure 4b shows one of the main results of the paper, that is the collected photon flux from a single molecule in the micro-dome device at low temperatures, as a function of pump power. The measurements are compared to the case of a nude NC and of a NC in the micro-dome device on silica. The detected photons correspond to the fraction emitted in the Stokes-shifted band, upon resonant pumping (see Experimental Section). For a given excitation power, the corresponding count rate is retrieved by recording the clicks on the detector at the resonance peak (see Figure 1b), without any correction factor.

However, in case indistinguishable photons from the ZPL are required, non-resonant excitation on low-density NCs can be employed[50–52] and a similar count rate can be estimated, based on the typical branching ratio for DBT:Ac into the ZPL (between 30% and 50%[32]). For each configuration, the variability in the emitter position within the crystal results in some statistical fluctuations in the measured count rate within nominally identical structures. The stronger effect is present in the dome-on-gold, as follows from the previous discussion on Figure 3. The direct comparison reported in Figure 4 is, however, representative of the typical observed trend.

As expected, a saturation curve is observed in all three cases as a function of the pump power, expressed in logarithmic scale. The detected counts are fitted according to the formula $R(P) = (a + bP) + R_\infty P/(P + P_s)$, with R_∞ being the maximum detected count rate, P the laser power, P_s the saturation power and $(a + bP)$ accounting for the residual laser scattering as a linear contribution. We obtain a maximum detected photon flux equal to $R_{\infty_{NC}} = (0.18 \pm 0.01)$ Mcps, $R_{\infty_{dome}} = (0.66 \pm 0.02)$ Mcps and $R_{\infty_{Au-dome}} = (2.38 \pm 0.11)$ Mcps, respectively. Dividing the latter value by the efficiency of the detector ($\eta_{det} \sim 65\%$), of the optical path (34%) and by the objective transmission (70%), one gets a maximum count rate at the first lens equal to about 15 Mcps. This corresponds to a collection efficiency for the micro-dome and the objective of about 40% (see Supporting Information for details on the calculations). This value is roughly compatible with the numerical results presented in Figure 3, taking into account the limits of the 2D approximation, some unavoidable scattering from surface roughness, deviation of the structure with respect to the nominal parameters, besides few percent losses in the

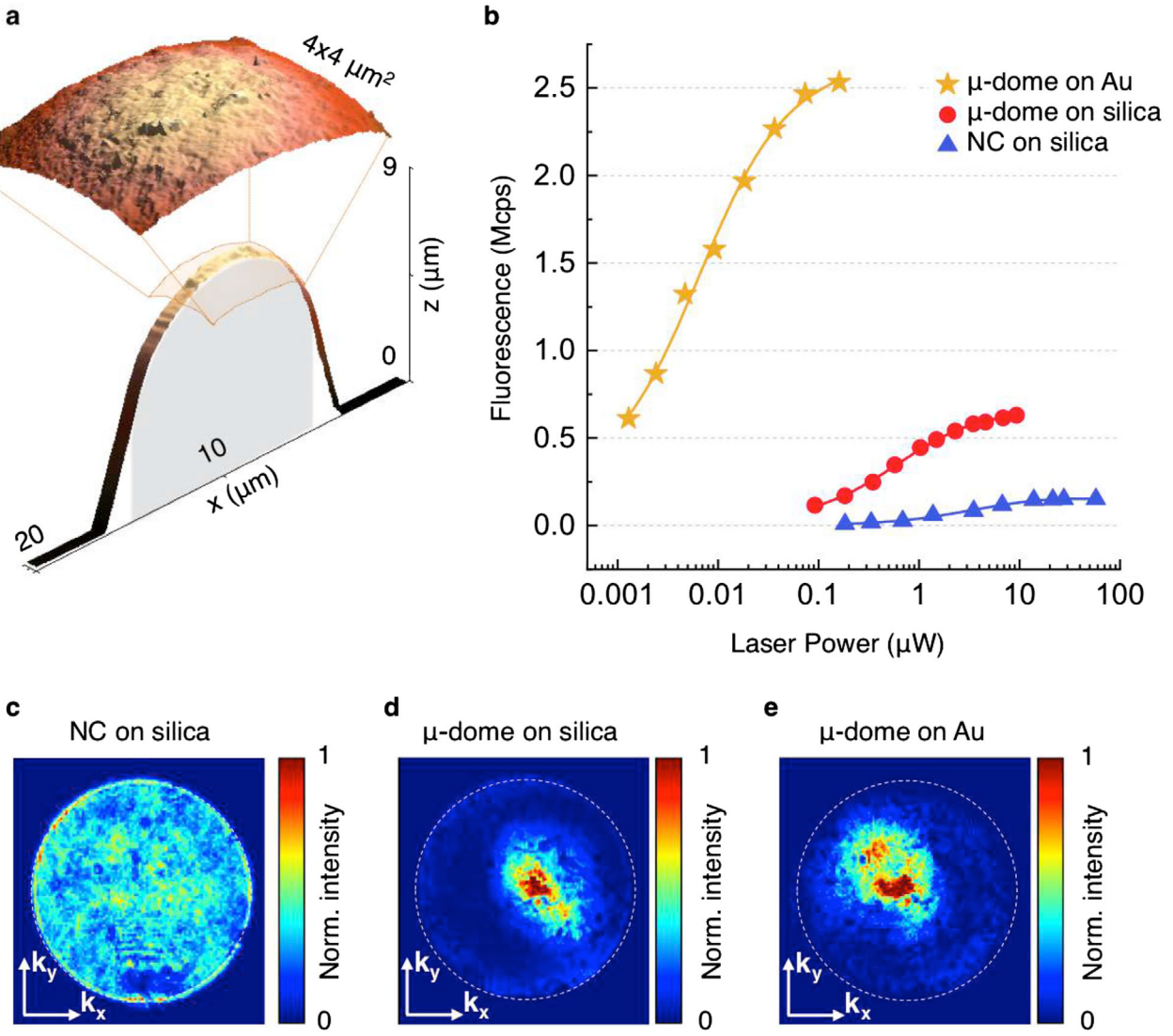

Figure 4. Enhanced collection from a single molecule. a) AFM characterization of the fabricated micro-dome on gold. The strip-scan of the structure passing through the dome pole gives an estimation of the experimental dimensions, in good agreement with the nominal values (grey silhouette). b) Experimental collected photon flux at low temperature from a single molecule embedded in the fabricated micro-dome structure on gold (yellow stars), compared to the case of the micro-dome on silica (red dots) and of the nude nanocrystal (blue triangles). The data are fitted (continuous lines) according to the formula $R(P) = (a + bP) + R_{\infty}P/(P + P_s)$. No background subtraction has been applied. c–e) Back focal plane (BFP) measurements of the emitted fluorescence, showing the emission pattern for the micro-dome on gold, the micro-dome on silica and the nude nanocrystal, respectively. The white dashed circumferences identify the experimental maximum collection angle of ~ 42°.

metal and in the quantum yield. The count rate from a single cold molecule in the optimized micro-dome design is to our knowledge the highest reported to date and appears particularly significant when associated with the long excited state lifetime of DBT molecules (≃ 4.2 ns). In particular, with respect to the nude nanocrystal, we measure a factor 3.7 ± 0.2 improvement in the collected photon flux for the micro-dome on silica, and a factor 13 ± 1 in the case of the optimal configuration for the micro-dome on gold. Moreover, a reduction in the saturation power by about two orders of magnitude is observed, passing from a value of (56 ± 10) W/cm^2 to (0.10 ± 0.02) W cm^{-2}. Indeed, the presence of the modified SIL has the primary effect of increasing the effective numerical aperture of the optical system, hence improving its focusing efficiency. The underneath reflective layer further increases the intensity at the emitter position for a given input power. We note that 100% of the fabricated micro-domes exhibit fluorescence signal. By taking into account the six devices on gold on which the saturation curve has been measured, a good success rate is achieved, with the maximum photon counts at the detector being always above 0.8 Mcps. This result can be further optimized by integrating fluorescence imaging capability in the DLW workstation, and by employing NCs doped with single-molecule concentration.

In order to probe the emission pattern of the devices, we perform imaging of the back focal plane (BFP) of the objective lens, which provides the power distribution in the momentum

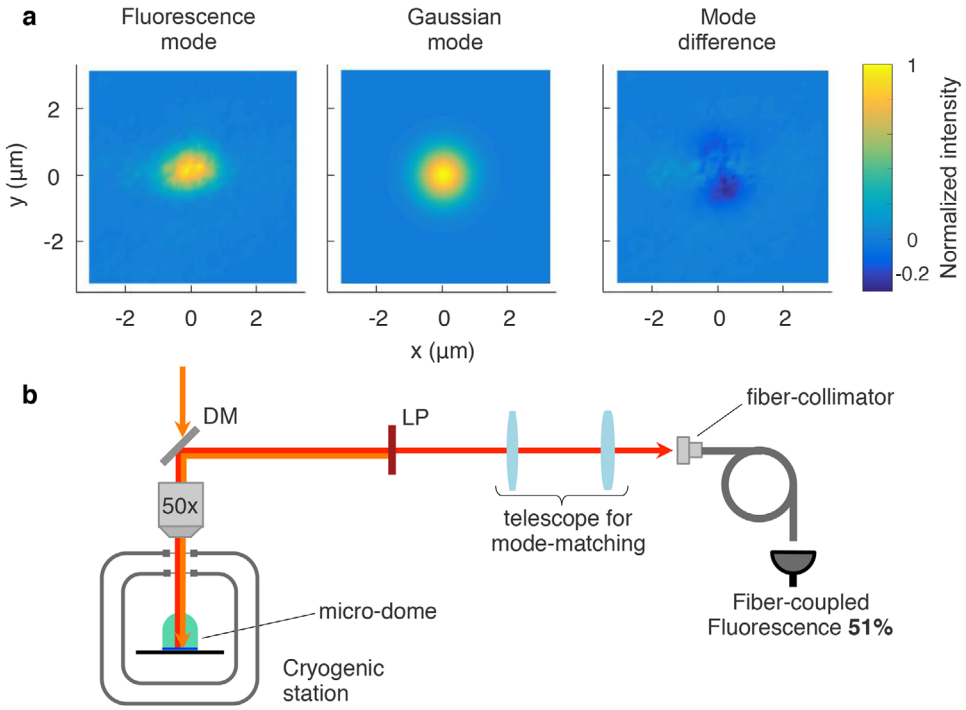

Figure 5. Efficient coupling into a fiber. a) The measured fluorescence spatial distribution of the integrated structure is compared to a Gaussian mode, typical of a single mode optical fiber, and the difference between the two profiles is shown on the right. b) Schematic of the fiber-coupling setup, which consists in the objective, a telescope and a tunable-distance fiber-collimator (DM and LP label the dichroic mirror and the long-pass filter respectively—see Experimental Section).

space of the emitted fluorescence. In Figures 4c–e, we compare the normalized BFP maps for the nude nanocrystal on silica, the micro-dome device on silica, and the micro-dome on gold. The white dashed circumferences in the plots identify the experimental maximum collection angle of $\sim 42°$, whereas the center of the circumference corresponds to the objective optical axis. Figure 4c shows a homogeneously bright map, as expected from a dipole emission and consistent with the typical on-plane orientation of the DBT:Ac system.[20,27] Conversely, Figure 4d,e confirms an effective redirection into small angles achieved in the micro-devices, competitive with what shown in much more complex structures.[53] In the last cases, the slight misalignment of the bright spots is evidence of the not perfectly centered emitter, which owes both to the DLW process and to the uncertainty in the fluorophore position within the Ac nanocrystal. Consistently with the results of the numerical simulations presented in Figure 3, the pattern of a micro-dome on gold with $\text{dipole}_h \simeq 100nm$ features most of its emission within the first 30° (see also Figure S1, Supporting Information). It is worth noticing that this configuration is not the one exhibiting the highest directivity. Narrower emission lobes can indeed be observed (see Figure S2, Supporting Information), corresponding though to a lower collection efficiency, as clearly evident from the central polar plot of Figure 3.

The effective redirection at narrow angles combined with the high detected count rate achieved with the micro-dome device are particularly suitable for the efficient coupling into a fiber, within the perspective of a compact fiber-coupled single photon source (SPS). With the experimental setup schematically shown in **Figure 5**b, a coupling efficiency up to 51% into a single mode fiber is achieved. The target value can be estimated in terms of mode matching, by comparing the measured fluorescence spatial distribution in the micro-dome on gold (Figure 5a) with a Gaussian mode, typical of a single mode optical fiber (Figure 5b). In particular, we estimate the best overlap integral to be of the order of $\simeq 80\%$, which suggests an upper bound for the expected coupling efficiency. Considering the flexibility offered by a polymeric photonic platform,[54] a monolitic fiber coupler can be integrated onto the metal-coated micro-dome in order to realize an alignment-free and ultra compact fiber-coupled SPS.

4. Conclusions

We have demonstrated the fast, efficient integration of single molecule quantum emitters in 3D polymeric structures, thus realizing a competitive organic photonic platform, leveraging the versatility of polymeric materials. The experimental results entail deterministic positioning of the source, fabrication on different substrates (dielectric, metallic) as well as integration in suspended designs. Furthermore, the compatibility of direct laser writing with organic nanocrystals is demonstrated by showing close-to Fourier-limited emission from a single embedded dibenzoterrylene molecule at 3 K. As a first example of the performance, we show enhanced collection efficiency for single organic emitters at low temperatures, reaching detected photon counts of 2.38 ± 0.11 Mcps, corresponding to about 15 Mcps at

the first lens. This value approximately doubles the state of the art for the detected count rate from a single molecule, with the improvement rising to a factor 5 considering the specific case of DBT.[55,56] The effective fluorescence redirection displayed in back-focal-plane measurements makes this device suitable for fiber-coupling, with an expected maximum efficiency of $\simeq 80\%$ and a measured value up to 50%.

The use of single-molecule emitters, characterized by a relatively small inhomogeneous broadening of about 0.1 nm, offers the appealing possibility of conveying indistinguishable photons from different remote sources.[26] Few-photon non-linearities can be also envisaged, based on such quantum emitters interacting with confined optical modes.[32,57] Owing to the great flexibility of the direct laser writing technique and to the versatility of polymeric materials, the proposed approach can be potentially extended to other PAH molecules, in order to couple them to monolithic cavities, waveguides and directional couplers. For example, a complex quantum effect such as the interference among more than two particles can be observed, using on-demand single photons generated by individual molecules embedded in 3D direct laser -written polymeric tritters.[58] On the other side, the proposed technology can be adapted for scalable and efficient coupling of multiple emitters, even in hybrid polymer-silicon nitride circuits.[11] Furthermore, the possibility to engineer photofunctional materials as photoresists[59] enables full customization, from the optimization of spatial resolution and mechanical stability, to the employment of photo-reactive[60] or electro-optical features for tuneable resonances. Thanks to its advantages, we expect that our platform will lead to a wealth of novel scalable micro-photonic devices with tailored functionalities, at the single emitter level.

5. Experimental Section

Sample Fabrication: The direct laser writing process was based on two-photon polymerization induced by a strongly focused laser beam. A commercial DLW workstation (Nanoscribe) and the commercially available negative-tone IP-photoresists (IPs) were employed. IPs provide high resolution and high mechanical stability for structures in the micro- and submicron range and are chemically compatible with the Ac crystalline matrix. Moreover they require low exposure and developing time for the writing process,[61,62] thus minimizing possible detrimental effects on DBT:Ac NCs. Finally, the choice of IPs was motivated by the absence of background fluorescence in the spectral range of the molecule emission.

The DBT:Ac NCs growth procedure consisted in injecting 250 µL of a mixture of 4 : 10^3 1 mM DBT-toluene and 5 mM Ac-acetone solutions into 5 mL of sonicating water. While continuously sonicating the system for 30 min, solvents dissolved in water and DBT:Ac crystals were formed in aqueous suspension, as described in detail in ref. [20]. Solvents and Ac were purchased from Sigma-Aldrich, water was deionized by a Milli-Q Advantage A10 system (resistivity of 18.2 $m\Omega \cdot cm$ at 25 °C), and DBT was purchased from Mercachem.

In the micro-dome configurations, the nanocrystals were deposited on a fused silica coverslip via dessication after drop-casting ~10 µL of the aqueous suspension. Before the deposition, the substrate was extensively cleaned with acetone and optical paper. In the micro-dome on gold configuration, the substrate was also sputter-coated with a ~200 nm thick gold film. After the deposition, NCs were protected from sublimation and from fabrication damage by spin-coating a 200 nm-thick layer of PVA (purchased from Sigma-Aldrich). To fabricate the micro-lens structures, the optimized geometry was translated into a series of concentric rings by an automated script which fitted the volumetric dimensions of the writing laser focus (the voxel, typically ellipsoidal and depending on laser power) to the target external surface dimensions and smoothness of the structure. 7.5 mW laser power was used, measured at the entrance of the objective. The translated rings were written directly in drop-cast IP-DIP (micro resist technology GmbH, $n = 1.54$) resist via dip-in DLW lithography (Nanoscribe GmbH). Each micro-dome was written on the top of a single nanocrystal by localizing it through the same microscope objective at the imaging feedback of the workstation. The total writing time for one micro-lens was ~20 min. The unexposed photoresist was eventually removed in a development bath of propylene glycol monomethyl ether acetate (PGMEA) for 5 min and then in isopropyl alcohol for 5 min. After development the sample was carefully dried with a weak and clean air flux.

For the suspended waveguide configuration, DBT:Ac NCs were dispersed in the photoresist such to be successively embedded in the suspended middlepoint of the structure. This was achieved by first spin-coating a layer of IP-G (micro resist technology GmbH, $n = 1.52$) resist of thickness ranging from 5 to 10 µm, upon which NCs were then deposited. This thickness was imposed by issues of mechanical stability and coupling efficiency, since waveguides bend and fall for thicknesses $\gtrsim$10 µm, while fluorescence is absorbed by the substrate and not efficiently guided for thicknesses $\lesssim$5 µm. The choice of IP-G was prescribed by the necessity of rigidity of the spin-coated layer in order to avoid sinking of the deposited NCs, and this was attained by pre-baking of IP-G at 100 °C for 30 min. Therefore, deposition of NCs was carried through the same procedure previously described, and followed by drop-casting of IP-DIP for total envelopment of the emitters. The suspended waveguide was then written in one step fabrication by localizing the nanocrystal, estimating its distance from the substrate via the piezo-system feedback of the workstation, and defining the suitable waveguide dimensions to be employed to effectively wrap the nanocrystal (the whole writing process requires about 5 min). In this case, the waveguide design was translated into a series of arch-like lines. Development and drying was performed as previously described.

Morphological Characterization: Topological images were performed by SEM (Phenom Pro, PhenomWorld) and AFM (home-built equipment based on piezo XYZ positioning system (PI-527.3CL from Physik Instrumente) and R9 controller (RHK Technology)) equipped with a soft silicon probe CSG01 (NTMDT). In particular, for SEM contrast images, after optical characterization, the samples were sputter-coated with a ~50 nm gold film.

Simulations: Numerical simulations of the collection efficiency for the non-integrated nanocrystal on silica and for the NC inside the micro-domes on silica and on gold respectively, were performed using a commercial software (Comsol Multiphysics) implementing the 2D Finite Element Method (FEM). The nanocrystal is modeled in each configuration as a 800 nm × 400 nm platelet of Ac ($n = 1.7$) with the molecules modelled as a line current orthogonal to the simulation plane and placed at the center of the nanocrystal, 100 nm from the substrate. In such configuration, the numerical results correctly modeled radiation in the orthogonal plane to the dipole, which is where most of the power was radiated (see ref. [46] for a 3D simulation of a similar structure). A layer of 200 nm of PVA ($n = 1.475$) covered the whole considered area, including the nanocrystal. In the integrated configurations the micro-dome consisted in a hemisphere of radius 5.3 µm placed on a cylindrical base with the same radius and height $h = 3.4$ µm. For the optimal configuration on reflective surface, the silica substrate was covered with a 180 nm-thick layer of gold. The collection efficiency was evaluated by integrating the far fields within the acceptance angle defined by the numerical aperture of our setup (42°), and normalizing by the integrated far fields on the whole 2π angle. The collected photon flux was calculated as the ratio between the power radiated by a dipole in the far field within the maximum acceptance angle given by the numerical aperture $NA \sim 0.62$ and the power radiated by the same dipole in a homogeneous medium with the refractive index of 1.7.

Optical Setup: The optical characterization of DBT molecules within the Ac NC was performed with a versatile home-built scanning fluorescence confocal microscope. The set-up was equipped with a closed-cycle helium cryostat (Cryostation by Montana Instruments), capable of cooling samples to 2.7 K. Molecules could be excited off-resonance at 767 nm by a CW external-cavity diode laser (Toptica DLX110) or alternatively at

cryogenic temperature with a resonant CW distributed feedback diode laser (Toptica, LD-0785-0080-DFB-1), which was centered at 784.6 nm and could be scanned continuously in frequency over a range of 800 GHz. All laser sources were fiber-coupled and linearly polarized by means of a half-wave plate in the excitation path to allow optimal coupling to single DBT transition. The laser intensities reported in the main text were calculated from the power measured at the objective entrance divided by the measured area of the confocal spot at the substrate. For low-temperature measurements, the excitation light was focused onto the sample by a glass-thickness- compensation air objective (OptoSigma 50×, $NA = 0.65$, $WD = 10.48$ mm) and could be scanned over the sample by a telecentric system and a dual-axis galvo-mirror. For room temperature measurements, a long-distance air objective (Mitutoyo 100× Plan Apochromat, $NA = 0.7$, $WD = 6$ mm) was used to focus light onto the sample, which was mounted on a piezoelectric nanopositioner (NanoCube by Physik Instrumente). The Stokes-shifted fluorescence was collected by the same microscope objective used in excitation, separated from the excitation light through a dichroic mirror (Semrock FF776-Di01) and a long-pass filter (Semrock RazorEdge LP02-785RE-25), and detected by either an EMCCD camera (Andor iXon 885, 1004 × 1002 pixels, pixel size 8 μm × 8 μm) or by a SPAD (Excelitas SPCM-AQRH-14-TR). The reported single-photon fluxes were retrieved deviding the measured counts at the SPAD by the efficiency of the SPAD ($\eta_{det} = 65\%$), by the objective transmission (70%), and by the efficiency of the optical path (34%), which accounts for the dichroic transmission at 785 nm and for the losses at metallic mirrors and spherical lenses. For the HBT configuration, two fibered SPADs (Excelitas SPCM-800-14-FC) and a time correlated single photon counting (TCSPC) card (PicoHarp 300 by PicoQuant) were employed. A converging lens could be inserted in the excitation path to switch between confocal and wide-field illumination, while a converging lens was added in the detection path before the EMCCD camera to study the wave-vector distribution of the light emitted by single DBT molecules via BFP imaging. For the fiber-coupling configuration, a single-mode fiber, an adjustable fiber-collimator and a free-space telescope were employed to match the fluorescence mode to the fiber. Measurements of laser throughput in the waveguides were performed by focusing the laser at one coupler, through the substrate, and evaluating the transmitted light at the opposite coupler. The measured signal was then normalized to the direct reflection of the input laser on a mirror. Finally, the value was corrected for the overlap integral between the laser spatial mode and the waveguide spatial mode, which were not optimally matched in the experiment.

Supporting Information

Supporting Information is available from the Wiley Online Library or from the author.

Acknowledgements

The authors acknowledge and thank Hengsbach Stefan and Bade Klaus from the Institute of Microstructure Technology (MIT) in Karlsruhe, for the useful discussions and insights on the fabrication process. This project has received funding from the EraNET Cofund Initiatives QuantERA within the European Union's Horizon 2020 research and innovation program grant agreement No. 731473 (project ORQUID), and from the project EMPIR 17FUN06 SIQUST. M.C. acknowledges the Karlsruhe Nano Micro Facility (KNMF) for the access to fabrication and characterization technologies within the KNMF proposals 2018-019-021009 and 2019-021-025773.

Conflict of Interest

The authors declare no conflict of interest.

Author Contributions

M.C., P.L., and C.T. conceived the research and designed the experiments. M.C. fabricated the devices with help from S.N. M.C., P.L., and M.T. carried out the experimental characterization. F.P., P.L., M.C. carried out the theoretical analysis. B.T. and M.C. performed the morphological characterization. C.T. supervised the project. All authors discussed the results. M.C. and C.T. wrote the manuscript with critical feedback from all authors.

Keywords

direct laser writing, integrated optics, quantum emitters, single molecules, single photon sources

Received: January 7, 2020
Revised: March 31, 2020
Published online: June 1, 2020

[1] J. Wang, F. Sciarrino, A. Laing, M. G. Thompson, *Nat. Photonics* **2020**, *14*, 273.
[2] B. Lounis, M. Orrit, *Rep. Prog. Phys.* **2005**, *68*, 1129.
[3] I. R. Berchera, I. P. Degiovanni, *Metrologia* **2019**, *56*, 024001.
[4] O. Benson, *Nature* **2011**, *480*, 193.
[5] A. Sipahigil, R. E. Evans, D. D. Sukachev, M. J. Burek, J. Borregaard, M. K. Bhaskar, C. T. Nguyen, J. L. Pacheco, H. A. Atikian, C. Meuwly, R. M. Camacho, F. Jelezko, E. Bielejec, H. Park, M. Lončar, M. D. Lukin, *Science* **2016**, *354*, 847.
[6] H. Thyrrestrup, G. Kiršanskė, H. Le Jeannic, T. Pregnolato, L. Zhai, L. Raahauge, L. Midolo, N. Rotenberg, A. Javadi, R. Schott, A. D. Wieck, A. Ludwig, M. C. Löbl, I. Söllner, R. J. Warburton, P. Lodahl, *Nano Lett.* **2018**, *18*, 1801.
[7] U. Jantzen, A. B. Kurz, D. S. Rudnicki, C. Schäfermeier, K. D. Jahnke, U. L. Andersen, V. A. Davydov, V. N. Agafonov, A. Kubanek, L. J. Rogers, F. Jelezko, *New J. Phys.* **2016**, *18*, 073036.
[8] J. Liu, K. Konthasinghe, M. Davanço, J. Lawall, V. Anant, V. Verma, R. Mirin, S. W. Nam, J. D. Song, B. Ma, Z. S. Chen, H. Q. Ni, Z. C. Niu, K. Srinivasan, *Phys. Rev. Applied* **2018**, *9*, 064019.
[9] J. J. Green, J. H. Elisseeff, *Nature* **2016**, *540*, 386.
[10] S. Nocentini, D. Martella, C. Parmeggiani, D. S. Wiersma, *Adv. Optical Mater.* **2019**, *7*, 1900156.
[11] M. Schumann, T. Bückmann, N. Gruhler, M. Wegener, W. Pernice, *Light: Sci. Appl.* **2014**, *3*, e175.
[12] N. Lindenmann, G. Balthasar, D. Hillerkuss, R. Schmogrow, M. Jordan, J. Leuthold, W. Freude, C. Koos, *Opt. Express* **2012**, *20*, 17667.
[13] A. W. Schell, J. Kaschke, J. Fischer, R. Henze, J. Wolters, M. Wegener, O. Benson, *Sci. Rep.* **2013**, *3*, 1577.
[14] A. W. Schell, T. Neumer, Q. Shi, J. Kaschke, J. Fischer, M. Wegener, O. Benson, *Appl. Phys. Lett.* **2014**, *105*, 231117.
[15] Q. Shi, B. Sontheimer, N. Nikolay, A. W. Schell, J. Fischer, A. Naber, O. Benson, M. Wegener, *Sci. Rep.* **2016**, *6*, 31135.
[16] M. Sartison, S. L. Portalupi, T. Gissibl, M. Jetter, H. Giessen, P. Michler, *Sci. Rep.* **2017**, *7*, 39916.
[17] S. Morozov, M. Gaio, S. A. Maier, R. Sapienza, *Nano Lett.* **2018**, *18*, 3060.
[18] A. Landowski, J. Gutsche, S. Guckenbiehl, M. Schönberg, G. von Freymann, A. Widera, *APL Photonics* **2020**, *5*, 016101.
[19] P. Frantsuzov, M. Kuno, B. Janko, R. A. Marcus, *Nat. Phys.* **2008**, *4*, 519.
[20] S. Pazzagli, P. Lombardi, D. Martella, M. Colautti, B. Tiribilli, F. S. Cataliotti, C. Toninelli, *ACS Nano* **2018**, *12*, 4295.

[21] K. G. Schädler, C. Ciancico, S. Pazzagli, P. Lombardi, A. Bachtold, C. Toninelli, A. Reserbat-Plantey, F. H. L. Koppens, *Nano Lett.* **2019**, *19*, 3789.
[22] C. Ciancico, K. G. Schädler, S. Pazzagli, M. Colautti, P. Lombardi, J. Osmond, C. Dore, A. Mihi, A. P. Ovvyan, W. H. P. Pernice, E. Berretti, A. Lavacchi, C. Toninelli, F. H. L. Koppens, A. Reserbat-Plantey, *ACS Photonics* **2019**, *6*, 3120.
[23] S. Kawata, H.-B. Sun, T. Tanaka, K. Takada, *Nature* **2001**, *412*, 697.
[24] Y.-L. Zhang, Q.-D. Chen, H. Xia, H.-B. Sun, *Nano Today* **2010**, *5*, 435.
[25] A. A. L. Nicolet, P. Bordat, C. Hofmann, M. A. Kol'chenko, B. Kozankiewicz, R. Brown, M. Orrit, *ChemPhysChem* **2007**, *8*, 1929.
[26] R. Lettow, Y. L. A. Rezus, A. Renn, G. Zumofen, E. Ikonen, S. Götzinger, V. Sandoghdar, *Phys. Rev. Lett.* **2010**, *104*, 123605.
[27] C. Toninelli, K. Early, J. Bremi, A. Renn, S. Götzinger, V. Sandoghdar, *Opt. Express* **2010**, *18*, 6577.
[28] M. Rezai, J. Wrachtrup, I. Gerhardt, *Optica* **2019**, *6*, 34.
[29] P. Lombardi, M. Trapuzzano, M. Colautti, G. Margheri, I. P. Degiovanni, M. López, S. Kück, C. Toninelli, *Adv. Quantum Technol.* **2020**, *3*, 1900083.
[30] J. Hwang, M. Pototschnig, R. Lettow, G. Zumofen, A. Renn, S. Götzinger, V. Sandoghdar, *Nature* **2009**, *460*, 76.
[31] A. Maser, B. Gmeiner, T. Utikal, S. Götzinger, V. Sandoghdar, *Nat. Photon.* **2016**, *10*, 450.
[32] D. Wang, H. Kelkar, D. Martin-Cano, D. Rattenbacher, A. Shkarin, T. Utikal, S. Götzinger, V. Sandoghdar, *Nat. Phys.* **2019**, *15*, 483.
[33] F. Troiani, A. Ghirri, M. Paris, C. Bonizzoni, M. Affronte, *J. Magn. Magn. Mater.* **2019**, 165534.
[34] V. Puller, B. Lounis, F. Pistolesi, *Phys. Rev. Lett.* **2013**, *110*, 125501.
[35] M. Croci, H.-J. Müschenborn, F. Güttler, A. Renn, U. P. Wild, *Chem. Phys. Lett.* **1993**, *212*, 71.
[36] S. Faez, P. Türschmann, H. R. Haakh, S. Götzinger, V. Sandoghdar, *Phys. Rev. Lett.* **2014**, *113*, 213601.
[37] Y. Tian, P. Navarro, M. Orrit, *Phys. Rev. Lett.* **2014**, *113*, 135505.
[38] G. Mazzamuto, A. Tabani, S. Pazzagli, S. Rizvi, A. Reserbat-Plantey, K. Schädler, G. Navickaite, L. Gaudreau, F. S. Cataliotti, F. Koppens, C. Toninelli, *New J. Phys.* **2014**, *16*, 113007.
[39] C. Toninelli, Y. Delley, T. Stoferle, A. Renn, S. Götzinger, V. Sandoghdar, *Appl. Phys. Lett.* **2010**, *97*, 021107.
[40] S. Checcucci, P. Lombardi, S. Rizvi, F. Sgrignuoli, N. Gruhler, F. B. Dieleman, F. S. Cataliotti, W. H. Pernice, M. Agio, C. Toninelli, *Light: Sci. Appl.* **2016**, *6*, e16245.
[41] S. M. Skoff, D. Papencordt, H. Schauffert, B. C. Bayer, A. Rauschenbeutel, *Phys. Rev. A* **2018**, *97*, 043839.
[42] P. Lombardi, A. Ovvyan, S. Pazzagli, G. Mazzamuto, G. Kewes, O. Neitzke, N. Gruhler, O. Benson, W. Pernice, F. Cataliotti, C. Toninelli, *ACS Photonics* **2017**.
[43] P. Türschmann, N. Rotenberg, J. Renger, I. Harder, O. Lohse, T. Utikal, S. Götzinger, V. Sandoghdar, *Nano Lett.* **2017**, *17*, 4941.
[44] S. Grandi, M. Nielsen, J. Cambiasso, S. Boissier, K. Major, C. Reardon, T. Krauss, R. Oulton, E. Hinds, A. Clark, *APL Photonics* **2019**, *4*, 086101.
[45] W. Barnes, G. Björk, J. Gérard, P. Jonsson, J. Wasey, P. Worthing, V. Zwiller, *Eur. Phys. J. D: At. Mol. Opt. Plasma Phys.* **2002**, *18*, 197.
[46] A. W. Schell, T. Neumer, O. Benson, *Opt. Lett.* **2014**, *39*, 4639.
[47] M. Kavaldzhiev, J. E. Perez, Y. Ivanov, A. Bertoncini, C. Liberale, J. Kosel, *Biomed. Phys. Eng. Express* **2017**, *3*, 025005.
[48] P. Kang, C. Chen, L. Hao, C. Zhu, Y. Hu, Z. Chen, *Mater. Res. Bull.* **2004**, *39*, 545.
[49] P. Siyushev, G. Stein, J. Wrachtrup, I. Gerhardt, *Nature* **2014**, *509*, 66.
[50] A. Kiraz, M. Ehrl, T. Hellerer, O. E. Müstecaplıoğlu, C. Bräuchle, A. Zumbusch, *Phys. Rev. Lett.* **2005**, *94*, 223602.
[51] J.-B. Trebbia, P. Tamarat, B. Lounis, *Phys. Rev. A* **2010**, *82*, 063803.
[52] M. Rezai, J. Wrachtrup, I. Gerhardt, *Phys. Rev. X* **2018**, *8*, 031026.
[53] E. Johlin, S. A. Mann, S. Kasture, A. F. Koenderink, E. C. Garnett, *Nat. Commun.* **2018**, *9*, 4742.
[54] T. Gissibl, S. Thiele, A. Herkommer, H. Giessen, *Nat. Photonics* **2016**, *10*, 554.
[55] C. Polisseni, K. D. Major, S. Boissier, S. Grandi, A. S. Clark, E. A. Hinds, *Opt. Express* **2016**, *24*, 5615.
[56] G. Wrigge, I. Gerhardt, J. Hwang, G. Zumofen, V. Sandoghdar, *Nat. Phys.* **2008**, *4*, 60.
[57] G. Kewes, M. Schoengen, O. Neitzke, P. Lombardi, R.-S. Schönfeld, G. Mazzamuto, A. W. Schell, J. Probst, J. Wolters, B. Löchel, C. Toninelli, O. Benson, *Sci. Rep.* **2016**, *6*, 28877.
[58] N. Spagnolo, C. Vitelli, L. Aparo, P. Mataloni, F. Sciarrino, A. Crespi, R. Ramponi, R. Osellame, *Nat. Commun.* **2013**, *4*, 1606.
[59] H. Kudo, T. Nishikubo, *Polym. J.* **2009**, *41*, 569.
[60] S. Nocentini, F. Riboli, M. Burresi, D. Martella, C. Parmeggiani, D. S. Wiersma, *ACS Photonics* **2018**, *5*, 3222.
[61] J. B. Mueller, J. Fischer, F. Mayer, M. Kadic, M. Wegener, *Adv. Mater.* **2014**, *26*, 6566.
[62] L. J. Jiang, Y. S. Zhou, W. Xiong, Y. Gao, X. Huang, L. Jiang, T. Baldacchini, J.-F. Silvain, Y. F. Lu, *Opt. Lett.* **2014**, *39*, 3034.